# Mathematical Modeling of Impacts of Patient Differences on Renin-Angiotensin System and Applications to COVID-19 Lung Fibrosis Outcomes

Mohammad Aminul Islam[a], Ashlee N. Ford Versypt[a,b,c,d,*]

[a]*Department of Chemical and Biological Engineering, University at Buffalo, The State University of New York, Buffalo, NY, 14260, USA*
[b]*Department of Biomedical Engineering, University at Buffalo, The State University of New York, Buffalo, NY, 14260, USA*
[c]*Institute for Artificial Intelligence and Data Science, University at Buffalo, The State University of New York, Buffalo, NY, 14260, USA*
[d]*Witebsky Center for Microbial Pathogenesis and Immunology, University at Buffalo, The State University of New York, Buffalo, NY, 14203, USA*

**Abstract**

Patient-specific premorbidity, age, and sex are significant heterogeneous factors that influence the severe manifestation of lung diseases, including COVID-19 fibrosis. The renin-angiotensin system (RAS) plays a prominent role in regulating the effects of these factors. Recent evidence suggests patient-specific alteration of RAS homeostasis concentrations with premorbidity and the expression level of angiotensin converting enzyme 2 (ACE2) during COVID-19. However, conflicting evidence suggests decreases, increases, or no changes in RAS after SARS-CoV-2 infection. In addition, detailed mechanisms connecting the patient-specific conditions before infection to infection-induced RAS alteration are still unknown. Here, a multiscale model is developed to quantify the systemic contribution of heterogeneous factors of RAS during COVID-19. Three submodels are connected—an ABM COVID-19 in-host lung tissue model, a RAS model, and a fibrosis model to investigate the effects of patient-group-specific factors in the systemic alteration of RAS and collagen deposition in the lung. The model results indicate cell death due to inflammatory response as a major contributor to the reduction of ACE and ACE2. In contrast, there are no significant changes in ACE2 dynamics due to viral-bound internalization of ACE2. Reduction of ACE and ACE2 downregulates the homeostasis concentration of RAS, including angiotensin II (ANGII), in the lung tissue. At the same time, the decrease in ACE2 increases systemic ANGII and results in severe lung injury and fibrosis. The model explains possible mechanisms for conflicting evidence of RAS alterations in previously published studies, and simulated results are consistent with reported RAS peptide values for SARS-CoV-2-negative and SARS-CoV-2-positive patients. We observed decreased RAS peptides for all virtual patient groups with aging in both sexes. In contrast, large variations in the magnitude of reduction were observed between male and female virtual patients in the older and middle-aged groups. We also predicted that feedback of ANGII•AT1R to renin could restore ANGI homeostasis concentration but fails to restore homeostasis values of RAS peptides downstream of ANGI. In addition, the results show that ACE2 variations with age and sex significantly alter the concentrations of RAS peptides and lead to collagen deposition with slight variations depending on age and sex. This model may find further applications in patient-specific calibrations of tissue models for acute and chronic lung diseases to develop personalized treatments.

*Keywords:* SARS-CoV-2, renin-angiotensin system, TGF-β, pulmonary fibrosis

## 1. Introduction

The renin-angiotensin system (RAS) has gained significant attention as alterations in RAS peptides and enzymes directly correlate with patient-specific premorbidity, age, and sex differences in response to COVID-19 lung diseases [1–4]. RAS is important in maintaining physiological processes, including blood pressure and vascular permeability [1]. The cascade of RAS's local and systemic regulatory processes begins with renin from the kidney and angiotensinogen (AGT) from the liver, which enter into the circulation through blood and migrate to the lung. The renin activity on AGT causes its conversion to angiotensin I (ANGI). ANGI uses the angiotensin converting enzyme (ACE), including ACE from the cell surface of lung tissue, to convert to angiotensin II (ANGII). ANGII binds with angiotensin converting enzyme 2 (ACE2) from the cell surface to form the ACE2•ANGII complex, which converts to angiotensin 1–7 (ANG1–7). ANGII also binds with angiotensin type 1 receptor (AT1R) and forms the ANGII•AT1R complex,

*Corresponding author at: 507 Furnas Hall, University at Buffalo, The State University of New York, Buffalo, NY 14260. Email address: ashleefv@buffalo.edu

which regulates the feedback signaling to the systemic renin production rate. In the subsequent reactions, ANGII binds with angiotensin type 2 receptor (AT2R) and forms the ANGII•AT2R complex, ANGII converts to angiotensin IV (ANGIV) by enzymatic reaction, and ANG1–7 binds with MAS receptor to form the MAS•ANG1–7 complex. The expressions of ACE2 [4] and homeostasis values of RAS peptides [5] are patient-dependent.

Kutz et al. [1] observed reductions in all RAS peptides and renin activity without significant differences in ACE and ACE2 activity in the serum of COVID-19 patients compared with matched controls. Contrarily, Liu et al. [2] reported increased ANGII in critically ill SARS-CoV-2 positive patients compared to non-critically ill SARS-CoV-2 positive patients. Another group observed increased plasma ANGII levels in SARS-CoV-2-infected patients compared to healthy individuals [6]. The up-regulation in ACE2 expression has also been observed in COVID-19 patients [7]. Contrary to all, Kintscher et al. [8] did not observe any significant differences in plasma RAS peptides and ACE2 activity between control and COVID-19 patients. To explain the conflicting data on RAS peptide alteration, Kutz et al. [1] highlighted the differences between their study and that of Liu et al. [2], particularly the selection of the baseline patient groups. The baseline patient group in Kutz et al. [1] was SARS-CoV-2-negative, whereas Liu et al. [2] selected SARS-CoV-2-positive patients with normal ANGII range. In addition to these contradictions and limitations of scarce patient data, detailed mechanisms suitable for explaining the conflicting observations in different patient groups still need to be determined.

Patient-specific premorbidity, age, and sex differences can account for response variations between patient groups. Pendergrass et al. [9] observed variations in RAS with sex differences for hypertensive rats. Xudong et al. [10] reported dramatically reduced ACE2 expression with aging and higher ACE2 content in old female rats than in males. In a recent mathematical study, Bastolla [11] showed a direct correlation between the severity of COVID-19 fatality depending on age and sex across three countries and experimental data for the expression of ACE2 from Xudong et al. [10]. Miesbach [12] reported that male patients were more affected by severe manifestations than female patients and depended on the activation of RAS and pathological roles of ANGII.

Downregulation of ACE2 inhibits the protective activity of downstream RAS peptides, resulting in inflammation and fibrosis [13, 14]. RAS regulates fibrosis by directly and indirectly activating and inhibiting latent transforming growth factor beta (TGF-β) [15]. ANGII•AT1R complex in RAS activates latent TGF-β directly or via Smad and ERK/p38/MAPK signaling pathways, whereas ANGII•AT2R complex inhibits TGF-β production. Via *in vitro* experiments, ANGII•AT1R was reported to induce procollagen synthesis from human fetal lung fibroblasts directly through mitogenesis and indirectly through TGF-β [16]. ANGII-induced TGF-β production was also observed in vascular smooth muscle cells [17] and glomerular mesangial cells [18]. In our earlier mathematical modeling work [19], we also identified TGF-β as a critical contributor to COVID-19 fibrosis. TGF-β activates and recruits macrophages and fibroblasts, and fibroblasts are responsible for excess collagen deposition and fibrosis [19–21].

Bleomycin-mouse models are widely used to evaluate the effect of RAS peptides and enzymes in lung fibrosis [22]. Li et al. [23] observed increased ANGII and collagen for ACE2 knockout mice in bleomycin-induced lung fibrosis models. Rey-Parra et al. [24] also ran similar experiments for ACE2 knockout male and female mice and observed increased collagen in both males and females with significantly increased collagen in males compared to females [24]; they also highlighted that a higher AT2R/AT1R ratio in female mice could be a possible explanation for the sex differences in collagen deposition. The bleomycin-induced lung fibrosis mouse model of Kuba et al. [25] showed increased ANGII in the presence of SARS-CoV spike proteins. Another study from the same lab reported that ACE2 knockout mice also increased ANGII [26]. The mouse model of Wang et al. [27] showed exogenous ACE2 attenuates bleomycin-induced lung injury by attenuating TGF-β production and collagen deposition.

Multiple computational and mathematical models have been developed to integrate and quantify some aspects of premorbidity, age, and sex differences in RAS and RAS-mediated fibrosis. Leete et al. [28] developed a mathematical model to investigate the impact of sex differences in RAS, and they identified ANGII•AT1R feedback mechanism as a significant modulator of sex differences. Pucci et al. [29] developed a mathematical model to investigate the pathogenic mechanisms of SARS-CoV-2 and RAS and applied their model for *in silico* testing of potential modulators to restore functionality. Sadria and Layton [30] expanded a RAS model with membrane-bound ACE2, shedding of ACE2, and internalized ACE2; connected that to a damage response model; and used the model to investigate the effects of drugs targeting ACE and AT1R. The mathematical modeling framework of Voutouri et al. [31] connected SARS-CoV-2 infection, RAS, innate and adaptive immune cells, and coagulation cascade to investigate the heterogeneity in treatment response and clinical outcome as a function of patient comorbidities, age, and immune response; the model predicted increases in ANGII in severe COVID-19 patients. Barbiero and Lió [32] developed a computational patient model integrating cardiovascular, RAS, and diabetic processes. They analyzed the effects of age, diabetes, and renal impairment during SARS-CoV-2 infection in a functional context. Our lab has also previously developed mathematical models of RAS for normal and impaired renal functions [33] and glucose dependency of RAS in diabetic kidney disease [34, 35].

Here, we developed a mathematical model that contributes to understanding patient-group-specific premorbidity,

age, and sex differences on RAS during SARS-CoV-2 infection. We connected a RAS model to our earlier agent-based model (ABM) framework for COVID-19 tissue response in the lung and fibrosis [19] to investigate and quantify the local and systemic effects of the patient-group-specific premorbidity, age, and sex differences on RAS in the progression of fibrosis due to SARS-CoV-2 infection.

## 2. Methods

### *2.1. COVID-19 RAS fibrosis model*

The COVID-19 RAS fibrosis model (Fig. 1) consists of three submodels: an ABM COVID-19 in-host lung tissue model to quantify tissue scale dynamics of ACE2 receptor trafficking and inflammatory immune response due to SARS-CoV-2 infection (submodel 1 in Fig. 1), a RAS model to account for patient-group-specific local and systemic changes of RAS peptides and enzymes (submodel 2 in Fig. 1), and a fibrosis model to quantify the effects of immune modulation by dysregulated RAS peptides and systemic contributions to lung fibrosis (submodel 3 in Fig. 1). We refer to the COVID-19 RAS fibrosis model as the "overall model." Each of the submodels is detailed in turn.

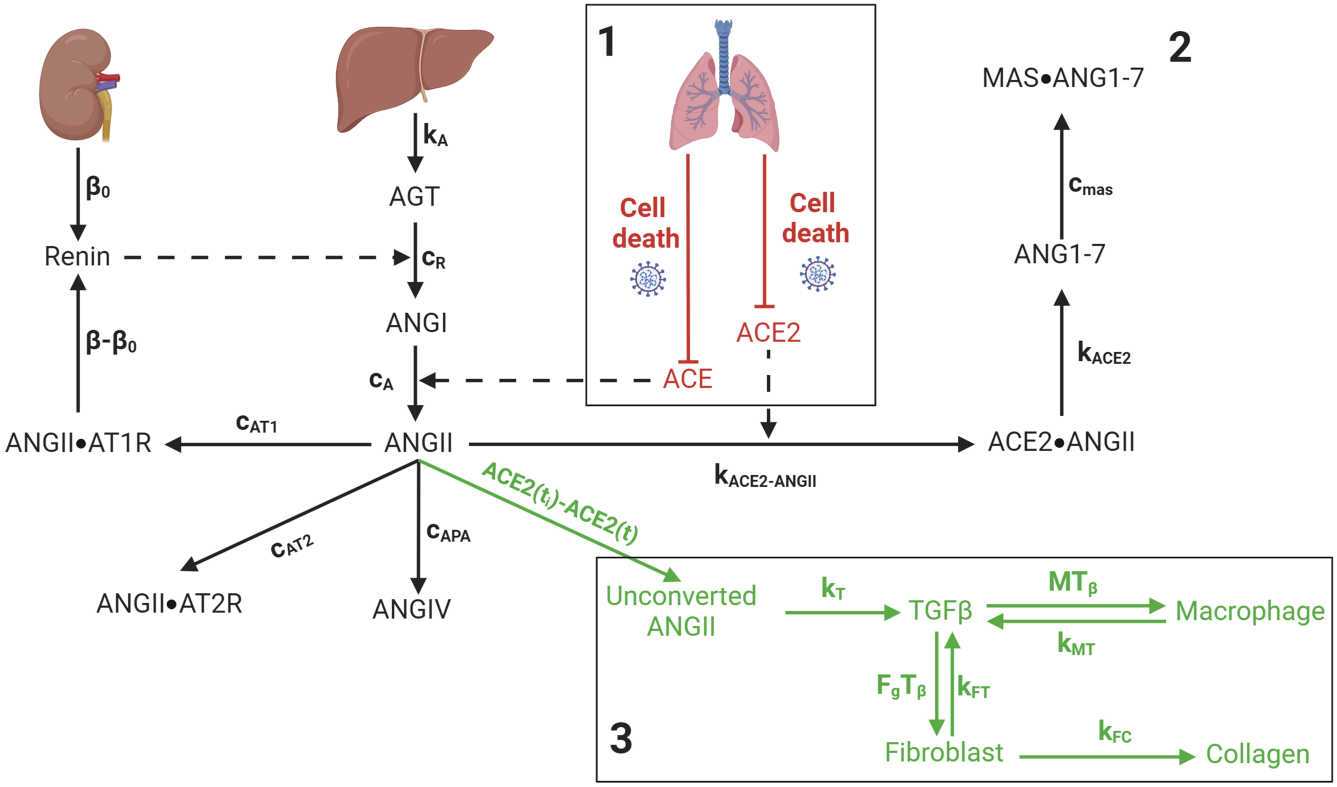


Fig. 1: Schematic diagram of COVID-19 renin-angiotensin system (RAS) fibrosis model. Three submodels are denoted by the numbers 1, 2, and 3, respectively, and separated by boxes. The number 1 denotes an agent-based model (ABM) of COVID-19 in-host lung tissue model, number 2 denotes a RAS model, and number 3 denotes a fibrosis model. Renin is produced from the kidney and angiotensinogen (AGT) from the liver. The renin activity on AGT causes its conversion to angiotensin I (ANGI). ANGI uses the angiotensin converting enzyme (ACE) from the cell surface of lung tissue to convert to angiotensin II (ANGII). ANGII binds with angiotensin converting enzyme 2 (ACE2) from the cell surface to form the ACE2•ANGII complex, which converts to angiotensin 1–7 (ANG1–7). ANGII also binds with angiotensin type 1 receptor (AT1R) and forms the ANGII•AT1R complex, which regulates the feedback signaling to the systemic renin production rate. In the subsequent reactions, ANGII binds with angiotensin type 2 receptor (AT2R) and forms the ANGII•AT2R complex, ANGII converts to angiotensin IV (ANGIV) by enzymatic reaction, and ANG1–7 binds with MAS1 proto-oncogene, G protein-coupled receptor (MAS) to form the MAS•ANG1–7 complex. During infection, the death of epithelial cells downregulates both ACE and ACE2, which increases unconverted ANGII. Unconverted ANGII induces transforming growth factor beta (TGF-β) production and activates the fibrosis cascade. Solid arrows denote transfer of one species to another, and dashed lines denote interactions that influence processes without being produced or consumed. All other notations are defined in Section 2.1 and Tables 1 and 2. Created with BioRender.com.

#### *2.1.1. COVID-19 tissue model*

In our earlier work, we developed a SARS-CoV-2 tissue simulator [19], which we call the "COVID-19 tissue model" (submodel 1 in Fig. 1). We use the model to determine the ACE and ACE2 receptor profiles. Here, we briefly recap the most salient features of the model.

The COVID-19 tissue model is developed in an open-source multiscale ABM framework PhysiCell [36] and simulates a tissue section of 800 $\mu m \times 800\ \mu m \times 20\ \mu m$, representing a monolayer of stationary epithelial cells on an alveolar surface of lung tissue. Initially, 2793 epithelial cells, 50 resident macrophages, 28 dendritic cells, and 57 fibroblasts are present in the simulated tissue. Using a uniform random distribution, we infect the simulated tissue by placing SARS-CoV-2 viral particles in the extracellular space. Viral particles diffuse through tissue and bind with unoccupied or unbound external ACE2 receptors (ueACE2) on the epithelial cell surfaces to form bound external ACE2 receptors (beACE2). These bound external ACE2 receptors internalize via endocytosis to form bound internal ACE2 receptors (biACE2), release the virions to form unbound internal ACE2 receptors (uiACE2), and recycle back to the cell surface.

The released virions from biACE2 replicate through intracellular viral replication kinetics, export back to the extracellular domain by exocytosis, and diffuse in the tissue. Our model considers the interactions between virion and ueACE2 as discrete events, whereas diffusion of the virus in tissue is continuous. Details of the intracellular virus model for replication kinetics, viral response, receptor trafficking, and rules for discrete to continuous transition of the virus are described in much greater detail in our earlier works [19, 37]. Viral infection activates the innate and adaptive immune response and recruits immune cells from the lymph nodes. Further immune and lymph node model details are available elsewhere [19, 37–39]. Viral infection and immune response activate latent TGF-β and shift the phenotype of pro-inflammatory M1 macrophages to anti-inflammatory M2 macrophages to produce TGF-β in the later phase of infection, which leads to fibroblast-mediated collagen deposition and fibrosis. Details of the effects of TGF-β sources in fibroblast-mediated collagen deposition at damaged sites of SARS-CoV-2 infected tissue are available in our earlier manuscript [19]. Here, we build upon that work to consider the effects of ACE2 receptor dynamics on the RAS network and lung fibrosis.

We assume the same initial number of ACE and ACE2 receptors. This assumption is based on the experimental observation of similar intensity of ACE and ACE2 protein expressions in lung tissue in the control mice experiments of Roca-Ho et al. [40]. Losses of ACE and ACE2 can occur due to epithelial cell death and binding between virus and ACE2 during SARS-CoV-2 infection. The simulated results from our tissue model suggested that loss of ACE2 mainly occurs due to cell death after the infection. Compared to that, loss of ACE2 due to viral binding is negligible due to the recycling of ACE2 receptors (details in Section 3.1). Since, ACE2 and ACE receptors are present in the cell surface and changes in ACE2 occur due to cell death, we assume that that changes in ACE and ACE2 are same. We use the dynamics of ueACE2 from the COVID-19 tissue model to account for the changes in ACE and ACE2, that is

$$ueACE2(t) = ACE(t) = ACE2(t) \tag{1}$$

*2.1.2. RAS model*

We developed a RAS model to account for patient-group-specific local and systemic changes of RAS peptides and enzymes during SARS-CoV-2 infection (submodel 2 in Fig. 1). In the model, the rate of change of renin is

$$\frac{d[R]}{dt} = \beta - \frac{\ln 2}{h_R}[R] \tag{2}$$

where $[R]$ is renin concentration, $\beta$ is the production rate, and $h_R$ is the half-life of renin. The term $\beta$ has two contributions: a constant source of renin from the kidney, $\beta_0$, and feedback of ANGII•AT1R to the production of renin, given by

$$\beta = \begin{cases} \beta_0, & \text{if no feedback} \\ \beta_0 + \left(\frac{[ANGII\cdot AT1R]_0}{[ANGII\cdot AT1R]}\right)^{\delta} - 1, & \text{else if } [ANGII\cdot AT1R] \geq [ANGII\cdot AT1R]_L \\ \beta_0 + \left(\frac{[ANGII\cdot AT1R]_0}{[ANGII\cdot AT1R]_L}\right)^{\delta} - 1, & \text{otherwise} \end{cases} \tag{3}$$

The feedback signaling depends on the initial concentration of ANGII•AT1R ($[ANGII\cdot AT1R]_0$), dynamics of ANGII•AT1R after infection ($[ANGII\cdot AT1R]$), and the lower threshold of ANGII•AT1R ($[ANGII\cdot AT1R]_L$). We estimated $[ANGII\cdot AT1R]_L$ based on the experimental study of Kutz et al. [1]. The strength of the feedback signaling is defined by a dimensionless number, $\delta$. The parameter values are listed in Tables 1 and 2.

The rate of change of AGT is

$$\frac{d[AGT]}{dt} = k_A - c_R\frac{ACE2(t)}{ACE2(t_i)}[R] - \frac{\ln 2}{h_A}[AGT] \tag{4}$$

where $[AGT]$ is concentration of AGT, $k_A$ is a constant source of AGT from the liver, $c_R$ relates renin concentration to its activity on AGT, $ACE2(t)$ is the ACE2 receptor profile determined from the COVID-19 tissue model and

described in Section 2.1.1, $ACE2(t_i)$ is the number of available ACE2 before time of infection ($t < t_i$), and $h_A$ is the half-life of AGT. Here, we consider plasma renin activity ($c_R$) based on earlier models [29, 41]. Kutz et al. [1] reported 58.5% reduction in plasma renin activity in COVID-19 patients. We also assume that changes in the $c_R$ scale are proportional to the ratio of changes in $ACE2(t)$ in the COVID-19 tissue model to account for the changes in plasma renin activity.

The rate of change of ANGI is

$$\frac{d[ANGI]}{dt} = c_R \frac{ACE2(t)}{ACE2(t_i)}[R] - c_A[ANGI]ACE(t) - \frac{\ln 2}{h_{A1}}[ANGI] \tag{5}$$

where $[ANGI]$ is the concentration of ANGI, $c_A$ is the rate constant for ACE catalyzed conversion of ANGI to ANGII, $ACE(t)$ is the ACE receptor profile determined from the COVID-19 tissue model and described in Section 2.1.1, and $h_{A1}$ is the half-life of ANGI.

The rate of change of ANGII is

$$\begin{aligned}\frac{d[ANGII]}{dt} &= c_A[ANGI]ACE(t) - c_{APA}[ANGII] - c_{AT1}[ANGII] - c_{AT2}[ANGII] \\ &\quad - k_{ACE2\cdot ANGII}[ANGII]ACE2(t) - \frac{\ln 2}{h_{A2}}[ANGII]\end{aligned} \tag{6}$$

where $[ANGII]$ is concentration of ANGII, $c_{APA}$ is the rate constant for APA catalyzed conversion of ANGII to ANGIV, $c_{AT1}$ and $c_{AT12}$ are the binding rate constants for formation of ANGII•AT1R and ANGII•AT2R, respectively, $k_{ACE2\cdot ANGII}$ is the binding rate constant for formation of ACE2•ANGII, $ACE2(t)$ is the ACE2 receptor profile determined from the COVID-19 tissue model and described in Section 2.1.1, and $h_{A2}$ is the half-life of ANGII.

The rates of change of ACE2•ANGII and ANG1–7 are

$$\frac{d[ACE2 \cdot ANGII]}{dt} = k_{ACE2\cdot ANGII}[ANGII]ACE2(t) - k_{ACE2}[ACE2 \cdot ANGII] \tag{7}$$

and

$$\frac{d[ANG1\text{–}7]}{dt} = k_{ACE2}[ACE2 \cdot ANGII] - c_{mas}[ANG1\text{–}7] - \frac{\ln 2}{h_{A17}}[ANG1\text{–}7] \tag{8}$$

where $[ACE2 \cdot ANGII]$ and $[ANG1\text{–}7]$ are concentrations of ACE2•ANGII and ANG1–7, respectively, $k_{ACE2}$ is the rate constant for the conversion rate of ACE2•ANGII to ANG1–7, $c_{mas}$ is the binding rate constant for the formation of MAS•ANG1–7, and $h_{A17}$ is the half-life of ANG1–7. Eqs. (7) and (8) are adapted from the mathematical model of Voutouri et al. [31]. Here, we consider the binding dynamics and reduction in ACE2 from the lung tissue model (Section 2.1.1) and no natural degradation of ACE2•ANGII.

The rate of change of ANGIV is

$$\frac{d[ANGIV]}{dt} = c_{APA}[ANGII] - \frac{\ln 2}{h_{A4}}[ANGIV] \tag{9}$$

where $[ANGIV]$ is concentration of ANGIV and $h_{A4}$ is the half-life of ANGIV.

ANGII binds with AT1R and AT2R receptors, and ANG1–7 binds with MAS receptors. The rates of change of these complexes are

$$\frac{d[ANGII \cdot AT1R]}{dt} = c_{AT1}[ANGII] - \frac{\ln 2}{h_{AT1}}[ANGII \cdot AT1R], \tag{10}$$

$$\frac{d[ANGII \cdot AT2R]}{dt} = c_{AT2}[ANGII] - \frac{\ln 2}{h_{AT2}}[ANGII \cdot AT2R], \tag{11}$$

and

$$\frac{d[MAS \cdot ANG1\text{–}7]}{dt} = c_{mas}[ANG1\text{–}7] - \frac{\ln 2}{h_{mas}}[MAS \cdot ANG1\text{–}7] \tag{12}$$

where $[ANGII \cdot AT1R]$, $[ANGII \cdot AT2R]$, and $[MAS \cdot ANG1\text{–}7]$ are concentrations and $h_{AT1}$, $h_{AT2}$, and $h_{mas}$ are the half lives of ANGII•AT1R, ANGII•AT2R, and MAS•ANG1–7, respectively.

The parameters $[R]_0$, $\beta$, $k_A$, $c_A$, $k_{ACE2\cdot ANGII}$, $k_{ACE2}$, $c_{APA}$, $c_{AT1}$, $c_{AT2}$, and $[MAS \cdot ANG1\text{–}7]_0$ in Eqs. (2)–(12) are patient-group-specific and require homeostasis concentration of RAS peptides and enzymes in calibration. A list of fixed parameters for the overall model is available in Table 1, and mean homeostasis RAS peptide concentrations for normotensive and hypertensive patients are listed in Table 2. We further calibrate the RAS model with the initial number of ACE and ACE2 receptors of virtual lung tissue in COVID-19 tissue model (Section 2.1.1). The patient-group-specific parameters for normotensive and hypertensive patients are calculated using the homeostasis values of RAS peptides and the initial number of ACE and ACE2 receptors from virtual lung tissue. We assume $c_{mas} = c_{AT2}$ and solve Eqs. (S1)–(S10) to calculate the patient-group-specific parameters (Table 2).

Table 1: List of fixed parameters for the overall model.

| Symbol | Definition | Value | Units | Source |
|---|---|---|---|---|
| submodel 1 | | | | |
| $DS$ | TGF-β activation rate from a damaged site | $2 \times 10^{-9}$ | ng min$^{-1}$ | Estimated in [19] |
| $MS$ | TGF-β secretion rate from an M2 macrophage | $2 \times 10^{-9}$ | ng min$^{-1}$ | Estimated in [19] |
| submodel 2 | | | | |
| $c_R$ | Renin activity on AGT | $2 \times 10^{1}$ | min$^{-1}$ | [29] |
| $h_R$ | Half-life of renin | $1.2 \times 10^{1}$ | min | [29, 41] |
| $h_A$ | Half-life of angiotensinogen | $6 \times 10^{2}$ | min | [29, 41] |
| $h_{A1}$ | Half-life of angiotensin I | $5 \times 10^{-1}$ | min | [29, 41] |
| $h_{A2}$ | Half-life of angiotensin II | $5 \times 10^{-1}$ | min | [29, 41] |
| $h_{A17}$ | Half-life of angiotensin 1–7 | $5 \times 10^{-1}$ | min | [29, 41] |
| $h_{A4}$ | Half-life of angiotensin IV | $5 \times 10^{-1}$ | min | Estimated |
| $h_{AT1}$ | Half-life of angiotensin II & receptor 1 complex | $1.2 \times 10^{1}$ | min | [29, 41] |
| $h_{AT2}$ | Half-life of angiotensin II & receptor 2 complex | $1.2 \times 10^{1}$ | min | [29, 41] |
| $h_{mas}$ | Half-life of angiotensin 1–7 & MAS complex | $1.20 \times 10^{1}$ | min | [29] |
| $\delta$ | Strength of feedback to Renin | $8 \times 10^{-1}$ [0, 1] | Unitless | [28, 29] |
| $[ANGII \cdot AT1R]_L$ | Lower threshold of ANGII·AT1R | 3 | fmol mL$^{-1}$ | [1] |
| submodel 3 | | | | |
| $k_T$ | ANGII-induced TGF-β production rate | $5.0 \times 10^{-4}$ | ng mL min$^{-1}$ fmol$^{-1}$ | Estimated |
| $k_{MT}$ | Macrophage TGF-β production rate | $4.86 \times 10^{-5}$ | min$^{-1}$ | [20, 21] |
| $k_{FT}$ | Fibroblast TGF-β production rate | $2.78 \times 10^{-6}$ | min$^{-1}$ | [20, 21] |
| $d_T$ | TGF-β degradation rate | $1.04 \times 10^{-2}$ | min$^{-1}$ | [20] |
| $d_M$ | Macrophage apoptosis rate | $4.17 \times 10^{-4}$ | min$^{-1}$ | [20, 21] |
| $d_F$ | Fibroblast apoptosis rate | $8.30 \times 10^{-5}$ | min$^{-1}$ | [20, 21] |
| $k_{FC}$ | Fibroblast collagen production rate | $2.52 \times 10^{-7}$ | μg min$^{-1}$ | Estimated from [42] |
| $V_{T\beta}$ | Rate parameter for TGF-β-dependent collagen deposition | $9.42 \times 10^{-1}$ | Unitless | Estimated in [19] from experimental data of [43, 44] |
| $k_{T\beta}$ | Saturation parameter for TGF-β-dependent collagen deposition | $1.74 \times 10^{-1}$ | Unitless | Estimated in [19] from experimental data of [43, 44] |
| $M(T_\beta)$ | TGF-β-dependent macrophage recruitment rate | interpolated | cell min$^{-1}$ | [45] |
| $F_g(T_\beta)$ | TGF-β-dependent fibroblast recruitment rate | interpolated | cell min$^{-1}$ | [45] |

Table 2: Homeostasis concentrations of species and parameter values in renin-angiotensin system (RAS) network for uninfected normotensive and hypertensive patients (submodel 2).

| Symbol | Definition | Hypertensive | Normotensive | Unit | Source |
|---|---|---|---|---|---|
| $[AGT]_0$ | angiotensinogen | $6 \times 10^{5}$ | $6 \times 10^{5}$ | fmol mL$^{-1}$ | [29, 46] |
| $[ANGI]_0$ | angiotensin I | 110 | 70 | fmol mL$^{-1}$ | [9, 29, 47] |
| $[ANGII]_0$ | angiotensin II | 156 | 28 | fmol mL$^{-1}$ | [9, 29, 47] |
| $[ANG1\text{–}7]_0$ | angiotensin 1–7 | 92 | 36 | fmol mL$^{-1}$ | [9, 29, 47, 48] |
| $ACE2_0$ | angiotensin converting enzyme 2 | 200–2000 | 200–2000 | cell$^{-1}$ | COVID-19 tissue model |
| $[ACE2 \cdot ANGII]_0$ | angiotensin II & ACE2 receptor complex | $2.1 \times 10^{4}$ | $2.1 \times 10^{4}$ | fmol mL$^{-1}$ | [31] |
| $[ANGIV_0]$ | angiotensin IV | 1 | 1 | fmol mL$^{-1}$ | [29, 49] |
| $[ANGII \cdot AT1R]_0$ | angiotensin II & type 1 receptor complex | 85 | 15 | fmol mL$^{-1}$ | [28, 29] |
| $[ANGII \cdot AT2R]_0$ | angiotensin II & type 2 receptor complex | 27 | 5 | fmol mL$^{-1}$ | [28, 29] |
| $[R]_0$ | Renin | $2.53 \times 10^{1}$ | $9.43 \times 10^{0}$ | fmol mL$^{-1}$ | calculated |
| $\beta_0$ | Renin production rate | $1.46 \times 10^{0}$ | $5.45 \times 10^{-1}$ | fmol mL$^{-1}$ min$^{-1}$ | calculated |
| $k_A$ | angiotensinogen production rate | $1.2 \times 10^{3}$ | $8.82 \times 10^{2}$ | fmol mL$^{-1}$ min$^{-1}$ | calculated |
| $c_A$ | ANGI to ANGII conversion rate | $1.15 \times 10^{-6}$ | $4.69 \times 10^{-7}$ | #ACE$^{-1}$ min$^{-1}$ | calculated |
| $k_{ACE2 \cdot ANGII}$ | ANGII & ACE2 receptor binding rate | $2.95 \times 10^{-7}$ | $6.43 \times 10^{-7}$ | #ACE2$^{-1}$ min$^{-1}$ | calculated |
| $k_{ACE2}$ | ANGII–ACE2 to ANG1–7 conversion rate | $6.12 \times 10^{-3}$ | $2.39 \times 10^{-3}$ | min$^{-1}$ | calculated |
| $c_{APA}$ | ANGII to ANGIV conversion rate | $8.89 \times 10^{-3}$ | $4.95 \times 10^{-2}$ | min$^{-1}$ | calculated |
| $c_{AT1}$ | ANGII & type 1 receptor binding rate | $3.15 \times 10^{-2}$ | $3.09 \times 10^{-2}$ | min$^{-1}$ | calculated |
| $c_{AT2}$ | ANGII & type 2 receptor binding rate | $1 \times 10^{-2}$ | $1.03 \times 10^{-2}$ | min$^{-1}$ | calculated |
| $[MAS \cdot ANG1\text{–}7]_0$ | angiotensin 1–7 & MAS receptor complex | $1.6 \times 10^{1}$ | $6.43 \times 10^{0}$ | fmol mL$^{-1}$ | calculated |

### *2.1.3. Fibrosis model*

We developed a fibrosis model to quantify the effects of immune modulation by dysregulated RAS peptides and systemic contributions to lung fibrosis (submodel 3 in Fig. 1). With less ACE2 in the lung, systemic ANGII is converted to ACE2·ANGII at a lower rate, providing some surplus of ANGII not converted along this pathway towards ANG1–7 and increase the systemic concentration of ANGII. We term the additional ANGII due to loss of ACE2 as "unconverted ANGII" and calculate the unconverted ANGII as

$$[U_{ANGII}](t) = k_{ACE2 \cdot ANGII}\big(ACE2(t_i)[ANGII]_0 - ACE2(t)[ANGII]\big) \tag{13}$$

where $[U_{ANGII}]$ is the concentration of unconverted ANGII, $[ANGII]_0$ is the homeostasis concentration of ANGII, $ACE2(t_i)$ is the number of available ACE2 before time of infection ($t < t_i$), $ACE2(t)$ is the number of available ACE2 during infection ($t \geq t_i$).

We assume that the unconverted ANGII modulates the direct and indirect activation of TGF-β, and we consider first-order reaction kinetics for ANGII-induced TGF-β production rate. Eq. (14) denotes the dynamics of TGF-β:

$$\frac{d[T_\beta]}{dt} = k_T[U_{ANGII}] + k_{MT}[M] + k_{FT}[F] - d_T[T_\beta] \tag{14}$$

where $[T_\beta]$ is TGF-β concentration, $k_T$ is ANGII-induced TGF-β production rate, $k_{MT}$ is TGF-β production rate from macrophages, $k_{FT}$ is TGF-β production rate from fibroblasts, and $d_T$ is degradation rate of TGF-β.

TGF-β-dependent macrophage recruitment rate ($M(T_\beta)$) and fibroblast recruitment rate ($F_g(T_\beta)$) are estimated from the experimental observations of Wahl et al. [45]. Linear interpolation is used for the missing ranges of data. Fig. S1 shows the dynamics of $M(T_\beta)$ and $F_g(T_\beta)$ with TGF-β. The population balances for macrophages and fibroblasts are

$$\frac{d[M]}{dt} = M(T_\beta) - d_M[M] \tag{15}$$

and

$$\frac{d[F]}{dt} = F_g(T_\beta) - d_F[F] \tag{16}$$

where $[M]$ and $[F]$ are the populations and $d_M$ and $d_F$ are the apoptosis rates of macrophages and fibroblasts, respectively.

The TGF-β-dependent collagen deposition rate from fibroblasts is

$$\frac{d[C]}{dt} = k_{FC}\frac{V_{T\beta}[T_\beta]}{k_{T\beta} + [T_\beta]}[C] \tag{17}$$

where $[C]$ is collagen concentration, $k_{FC}$ is the collagen production rate from fibroblasts, and $V_{T\beta}$ and $k_{T\beta}$ are corresponding rate and saturation parameters defining the TGF-β dependency on collagen deposition [19].

In the fibrosis model, we use the same parameters as our earlier work [19] except parameter values for TGF-β activation rate from a damaged site ($DS$) and TGF-β secretion rate from an M2 macrophage ($MS$) are fixed (Table 1), and the initial number of ACE2 receptors per cell is varied ($ueACE2_0$, Table 3) to represent virtual patient groups. The initial values of the COVID-19 tissue model and fibrosis model variables (Table 3) are all relative to changes from the baseline of an uninfected patient rather than absolute numbers and concentrations.

Table 3: Initial conditions for COVID-19 tissue and fibrosis submodels.

| Symbol | Definition | Initial condition | Unit |
|---|---|---|---|
| submodel 1 | | | |
| $ueACE2_0$ | Unoccupied external ACE2 receptors | 200–2000 | # |
| $beACE2_0$ | Virus-bound external ACE2 receptors | 0 | # |
| $biACE2_0$ | Virus-bound internal ACE2 receptors | 0 | # |
| $ueACE2_0$ | Unoccupied internal ACE2 receptors | 0 | # |
| submodel 3 | | | |
| $T_{\beta 0}$ | Initial concentration of TGF-β | 0 | ng mL$^{-1}$ |
| $M_0$ | Initial number of macrophages | 0 | cells |
| $F_0$ | Initial number of fibroblasts | 0 | cells |
| $C_0$ | Initial amount of collagen | 0 | µg |

### *2.2. Model validation*

Kutz et al. [1] studied patient data to investigate RAS peptide alteration between SARS-CoV-2-positive and SARS-CoV-2-negative patients with respiratory infections. The study design included older adults with premorbid conditions, such as hypertension, diabetes, and obesity, for both SARS-CoV-2-positive and SARS-CoV-2-negative patients. They observed lower equilibrium serum RAS peptides and plasma renin activity in SARS-CoV-2-positive patients compared to SARS-CoV-2-negative patients. They also reported the ranges of variations in ANGI (3–595 pmol L$^{-1}$), ANGII (10–1687 pmol L$^{-1}$), and ANG1-7 (3–166 pmol L$^{-1}$) in SARS-CoV-2-negative patients and the ranges of variations in ANGI (2.7–188 pmol L$^{-1}$), ANGII (2.1–357 pmol L$^{-1}$), and ANG1-7 (3–7.3 pmol L$^{-1}$) in SARS-CoV-2-positive patients. However, the time points for the data were not reported.

Here, the effects of variations in the initial values of RAS peptides are investigated. We sample the initial values of ANGI, ANGII, and ANG1-7 using log uniform distribution within the ranges of experimentally observed values of SARS-CoV-2-negative patients [1]. Also, we account for the relative differences in the initial values of ANGI, ANGII, and ANG1-7 by sampling within the bounds

$$[ANGII]_0 \geq \gamma_1[ANGI]_0 \cap [ANGII]_0 \geq \gamma_2[ANG1-7]_0 \cap [ANGI]_0 \geq \gamma_3[ANG1-7]_0 \tag{18}$$

where $\gamma_1$ is the ratio of ANGII to ANGI, $\gamma_2$ is the ratio of ANGII to ANG1-7, and $\gamma_3$ is the ratio of ANGI to ANG1-7. We selected $\gamma_1 = 1.4$, $\gamma_2 = 1.7$, and $\gamma_3 = 1.2$ using the homeostasis RAS peptides concentration for hypertensive patients listed in Table 2.

ANGIV, ANGII·AT1R, and ANGII·AT2R peptides are derived from ANGII. So, the variations in the initial values of ANGII also affect the initial values of ANGIV, ANGII·AT1R, and ANGII·AT2R. The concentrations of ANGIV,

ANGII·AT1R, and ANGII·AT2R are scaled based on ANGII value for hypertensive patients listed in Table 2 and new ANGII values are sampled from the distribution. For a sampled ANGII value ($[ANGII]_{0,s}$) and ANGII value for hypertensive patients listed in Table 2 ($[ANGII]_0$), we calculate the scaling factor $S_f$ as

$$S_f = 1 + \frac{[ANGII]_{0,s} - [ANGII]_0}{[ANGII]_0} \tag{19}$$

After that, $[ANGIV]_0$, $[ANGII \cdot AT1R]_0$, and $[ANGII \cdot AT2R]_0$ from Table 2 are multiplied with $S_f$ from Eq. (19).

### *2.3. Sensitivity analysis*

We use dynamic local sensitivity analysis for submodel 2 parameters (Section 2.1.2) to quantify the input parameters that significantly affect the output variables. We evaluate the changes in output variables with respect to the one-at-a-time variation of each model parameter. Nominal input values ($I_s$) are the parameter values calculated using patient-group-specific homeostasis concentrations of RAS peptides (Table 2). Nominal output values ($O_s(t)$) are the concentrations of RAS species at time $t$ using the parameters in Tables 1 and 2. The input parameter are multiplied by a multiplier ($m_S$) to change one input at a time. We calculate the change of new input value ($I_n$) as: $\Delta I = I_n - I_s$ where $I_n = m_S I_s$. The model for normalized sensitivity index, ($S_{k,t}$), for the predicted new output value ($O_n(t)$) is

$$\begin{aligned} S_{k,t} &= \frac{\Delta O(t)}{O_s(t)} \frac{I_s}{\Delta I} \\ &= \frac{O_n(t) - O_s(t)}{O_s(t)} \frac{1}{m_S - 1} \end{aligned} \tag{20}$$

where $k$ denotes parameters or variables, and $t$ denotes time. We apply additional rules to avoid division by zero, as described in Eq. (21).

$$S_{k,t} = \begin{cases} \frac{O_n(t) - O_s(t)}{O_s(t)} \frac{1}{m_S - 1}, & \text{if } O_s(t) \neq 0 \\ \frac{O_n(t)}{m_S - 1}, & \text{otherwise} \end{cases} \tag{21}$$

### *2.4. Data extraction*

Experimental data from the literature used in this paper were extracted from graphs in the sources (referenced in the text) using the web-based program WebPlotDigitizer [50].

### *2.5. Computational implementation*

All the simulations are performed in a Dell Precision 3640 tower workstation: Intel Core Processor i9–10900K (10 core, 20 MB cache, base 3.7 GHz, up to 5.3GHz, and 32GB RAM) using hyperthreading, for 6 total execution threads. For the ABM COVID-19 in-host lung tissue model (submodel 1), we use PhysiCell (Version 1.9.0) [36], with BioFVM [51] to solve the transport equations (details in Section 2.1.1). For a single run of submodel 1 with 21,600 minutes of simulation, the total wall clock time is around 18 minutes. We use Python 3.8 and odeint function in the scipy library to solve the differential equations in the RAS model and fibrosis model (submodel 2 and 3, details in Sections 2.1.2 and 2.1.3). The code for our earlier fibrosis model is available in a repository at `https://github.com/ashleefv/covid19fibrosis` [52]. The code for the COVID-19 RAS fibrosis model is available in a repository at `https://github.com/ashleefv/covid19fibrosisRAS` [53].

## 3. Results and Discussion

The overall model has three submodels. First, we infected the virtual lung tissue considering different initial numbers of ACE2 per cell ($ueACE2_0$) using the COVID-19 tissue model (submodel 1 in Section 2.1.1). The model was used to evaluate the dynamics of ACE2 receptors after SARS-CoV-2 infection. Sequentially, we calibrated the RAS model (submodel 2 in Section 2.1.2) with patient-group-specific homeostasis peptide concentrations from Table 2 and an initial number of ACE2 receptors from the COVID-19 tissue model (submodel 1 in Section 2.1.2). The model was used to simulate the dynamics of RAS peptides before infection. Then, the predicted ueACE2 dynamics from the submodel 1 were used as input for ACE and ACE2 dynamics in the submodel 2. Here, we quantified the effects of patient-group-specific premorbidity by varying initial RAS peptides concentration and the impact of age and sex by varying initial numbers of ACE2. Finally, we extended the model to investigate the effect of dysregulation in RAS peptides on COVID-19 lung fibrosis outcomes (submodel 3 in Section 2.1.3).

### 3.1. Dynamics of ACE2 and tissue damage after SARS-CoV-2 infection depends on initial number of ACE2

In our earlier COVID-19 tissue model [19], we considered a constant initial number of ACE2 per cell ($ueACE2_0 = 1000$). Here, we varied $ueACE2_0$ in each cell 200–2000 with an interval of 200 to account for age and sex differences. Since recent studies showed a direct correlation between ACE2 expression and COVID-19 fatality where male patients were more affected compared to female patients [11, 12], we selected the age and sex of our virtual patient cohort based on the tissue damage dynamics (Figs. S2 and S3). The lower ranges of $ueACE2_0$ represent older adults (200–800), intermediate ranges represent middle-aged (800–1200), and upper ranges of $ueACE2_0$ represent young patients (1200–2000). The variations of $ueACE2_0$ within a specific age group account for sex differences. ACE2 expression in the female rat lung was higher than in male rats [10, 11]. So, we selected that, within a specific age group, lower $ueACE2_0$ represents male, and higher $ueACE2_0$ represents female.

Figs. 2, S2, and S3 show the dynamics of the epitelial cell populations, ACE2 receptors, and tissue damage with variations in $ueACE2_0$. ACE2 reached a new steady state when removal of virions from the system occurred around six days. The effect of changes in ueACE2 is higher with lower $ueACE2_0$ as the number of available ACE2 and steady-state value of ACE2 after infection gets closer to zero (Fig. 2B, F, and J). There weren't any significant variations in ACE2 dynamics due to viral binding and internalization of ACE2 (beACE2, biACE2, and uiACE2, details in Section 2.1.1) as the recycling process moved a portion of internalized ACE2 back to the surface and there was ample availability of surface ACE2 receptors in neighboring uninfected cells (Fig. 2C, G, and K). However, a direct correlation between the dynamics of total number of epithelial cells and ueACE2 was observed, and they completely overlap when normalized (Fig. 2D, H, and L). The findings suggest that the dysregulation of ACE2 in the lung tissue will mainly occur due to the loss of major sources of ACE2 by the death of epithelial cells during infection. We also observed complete destruction of tissue for $ueACE2_0 \leq 600$, increased cell survivability for the range $600 \leq ueACE2_0 \leq 1000$, and steady behavior for $ueACE2_0 \geq 1000$ (Fig. S3).

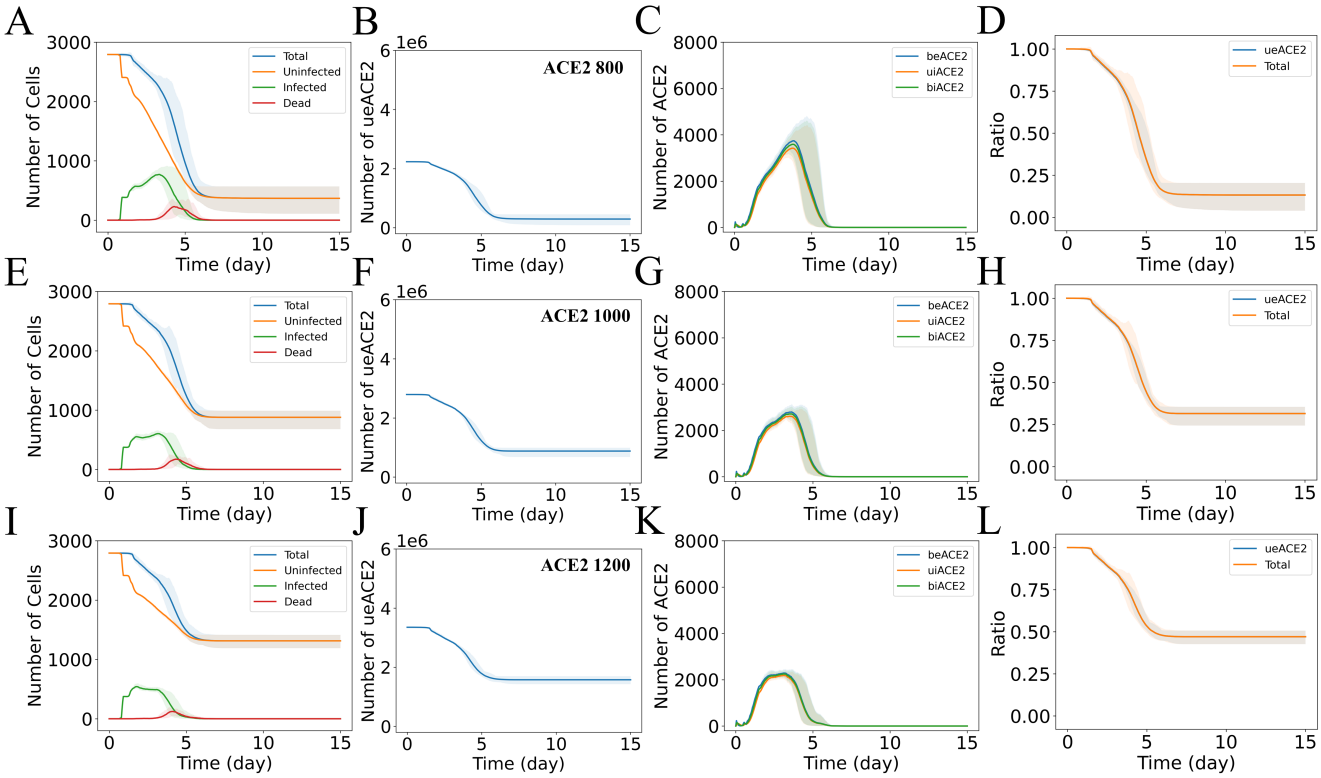


Fig. 2: Epithelial cells and ACE2 response to the different initial values of ACE2 ($ueACE2_0$). Dynamics of (A, E, I) total, uninfected, infected, and dead epithelial cells, (B, F, J) unbound external ACE2 (ueACE2), (C, G, K) bound external ACE2 (beACE2), bound internal ACE2 (biACE2), unbound internal ACE2 (uiACE2), and (D, H, L) normalized comparison between the dynamics of ueACE2 and total cells. Each row represents a fixed initial ueACE2 number ranging from 800–1200 per cell, top to bottom. The number of ueAce2 in the y-axis of B, F, and G denotes the total ueACE2 in the virtual lung tissue. The solid curves represent the means, and shaded areas represent the 5th and 95th percentiles of 15 iterations.

### 3.2. Dynamics of RAS peptides with variations in ACE2

As described earlier, we calibrated the submodel 2 (Section 2.1.2) with $ueACE2_0$ from the submodel 1 (Section 2.1.2) at the uninfected condition. We ran the submodel 2 for one day to calibrate the parameters of RAS for different patient groups. After one day of calibration, we used the ACE2 dynamics from submodel 1 as input in submodel 2 to simulate the dynamics of RAS species during infection. Submodel 2 was simulated for ten days post infection as ACE2 reached a new steady state around six days after infection.

Here, we considered hypertensive patients with no feedback of ANGII•AT1R to the production of renin. Figs. 3 and S4 show the dynamics of RAS peptides. We observed decreased ANGI and downstream peptides for all patient groups with aging in both sex groups. The magnitude of the reduction is largest for older patients ($ueACE2_0$ = 200–800), intermediate for middle-aged ($ueACE2_0$ = 800–1200), and smallest for younger patients ($ueACE2_0$ = 1200–2000). We also observed large variations in the magnitude of reduction between male and female patients in the older and middle-aged groups. In contrast, the variations due to sex were relatively slight for the young patient group.

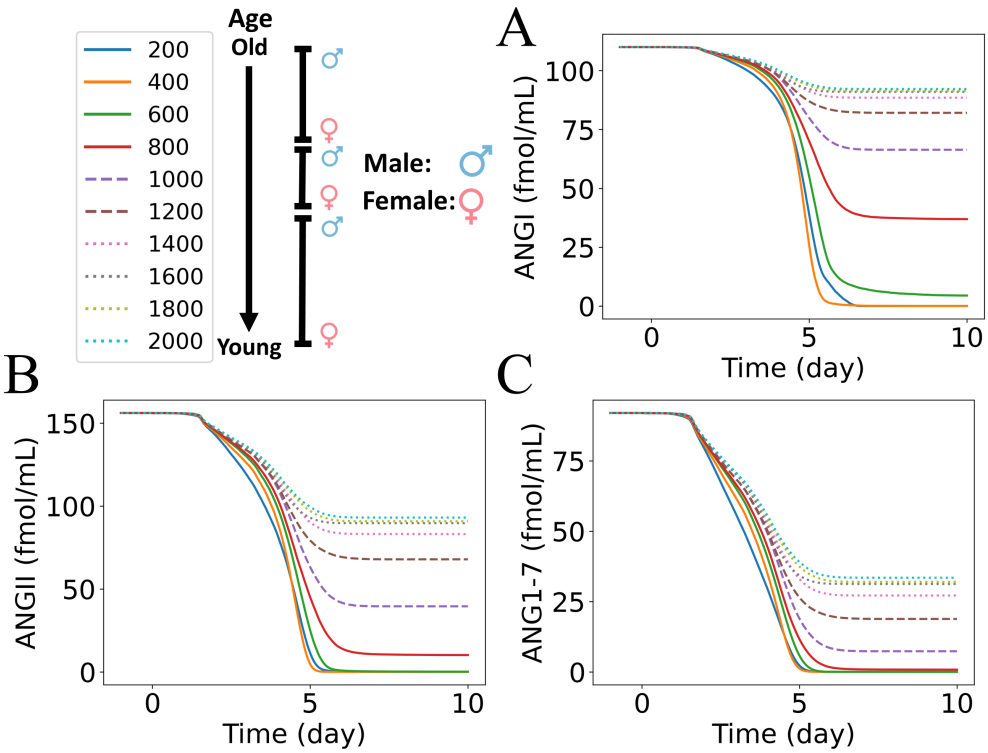


Fig. 3: Dynamics of RAS peptides with initial unbound external ACE2 ($ueACE2_0$). Dynamics of (A) ANGI, (B) ANGII, and (C) ANG1-7 for $ueACE2_0$ ranges of 200–2000.

### 3.3. Model predictions for experimentally observed decrease of RAS

We sampled 1000 sets of initial values of ANGI, ANGII, and ANG1-7 using log uniform distribution within the ranges of experimentally observed values of SARS-CoV-2-negative patients [1] (details in Section 2.2). We used ANGI ranges of 2–600 fmol mL$^{-1}$, ANGII ranges of 2–1700 fmol mL$^{-1}$, and ANG1-7 ranges of 2–150 fmol mL$^{-1}$ satisfying the bounds in Eq. (18). For a sampled ANGII value, scaling factor ($S_f$) was calculated using Eq. (19). Then, homeostasis concentration of $[ANGIV]_0$, $[ANGII \cdot AT1R]_0$, and $[ANGII \cdot AT2R]_0$ for hypertensive patients from Table 2 were multiplied with $S_f$. Fig. 4A–C show the dynamics of ANGI, ANGII, and ANG1-7 for 1000 sets of initial values. Fig. 4D–F are the subsets of Fig. 4A–C where the reduction in ANGI, ANGII, and ANG1-7 were in similar ranges of experimentally observed values of SARS-CoV-2-positive patients at ten days post infection. Our simulated results showed the dynamics of 65 virtual patients in Fig. 4D–F that were consistent with experimentally reported values of SARS-CoV-2-negative and SARS-CoV-2-positive patients.

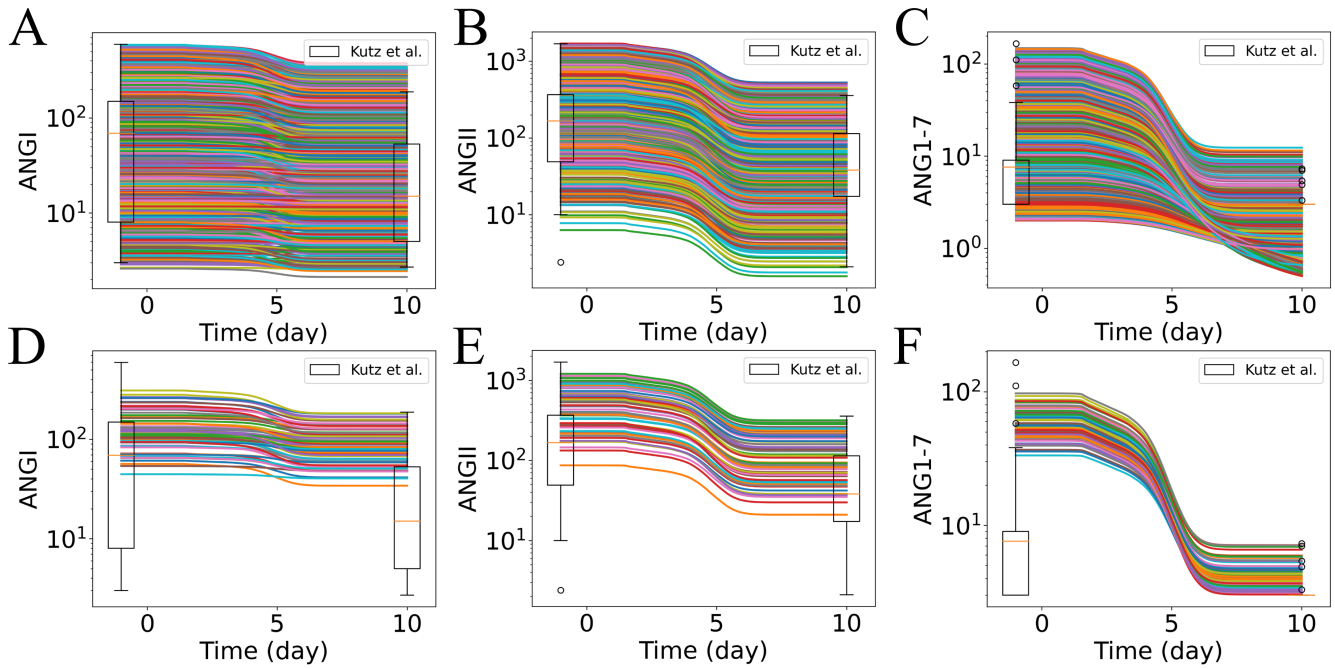


Fig. 4: Effect of initial values of ANGI, ANGII, and ANG1-7 in the dynamics of RAS peptides. (A, B, C) Initial values of ANGI, ANGII, and ANG1-7 were sampled within the experimentally observed ranges of SARS-CoV-2-negative patients reported in Kutz et al. [1] at one day before infection ($t = -1$ day). (D, E, F) The subset of the curves from the corresponding figure in the top row that show simular reduction within the experimentally observed ranges of SARS-CoV-2-positive patients reported in Kutz et al. [1] at ten days post-infection. The subset was selected if simulated dynamics of all three ANGI, ANGII, and ANG1-7 were within the experimental range simultaneously at ten days post-infection.

### *3.4. Effect of feedback from ANGII·AT1R to renin*

We investigated the effect of feedback from ANGII·AT1R to renin for hypertensive and normotensive patients. Neubauer et al. [54] reported no evidence for direct feedback of ANGII·AT1R to renin in the mouse kidney. They suggested that feedback of ANGII·AT1R to renin originates from *in vitro* experiments, and in their *in vivo* settings, the required concentrations of ANGII to induce renin secretion from renin cells were not achieved. Instead, the experimental study proposed an indirect effect of ANGII on renin-secreting cells (e.g., blood pressure) [54]. In contrast, Leete et al. [28] suggested the feedback strength of ANGII·AT1R to renin as the major difference between male and female RAS. Here, we investigated the response with and without feedback, and did not vary the strength of the feedback signaling ($\delta$) for the cases with feedback. We considered four virtual patient groups:

- Group 1: hypertensive patients with no feedback from ANGII·AT1R to renin
- Group 2: normotensive patients with no feedback from ANGII·AT1R to renin
- Group 3: hypertensive patients with feedback from ANGII·AT1R to renin
- Group 4: normotensive patients with feedback from ANGII·AT1R to renin

Fig. S5 shows the dynamics of RAS peptides, and Figs. 5 and S6 show the dose-response of ueACE2 to RAS peptides at 10 days post infection. We observed a similar magnitude of reduction between normotensive and hypertensive patients without feedback (Group 1 and Group 2 in Fig. 5) and with feedback (Group 3 and Group 4 in Fig. 5). However, the feedback of ANGII·AT1R to renin was able to restore the ANGI concentration to the homeostasis level for both hypertensive (Group 1 and Group 3 in Fig. 5) and normotensive (Group 2 and Group 4 in Fig. 5) middle-aged and younger patients. So, feedback of ANGII·AT1R to renin could restore ANGI homeostasis. Although the feedback signaling increased the ANGII concentration slightly compared to the cases without feedback signaling, no variations were observed in RAS peptides downstream of ANGII.

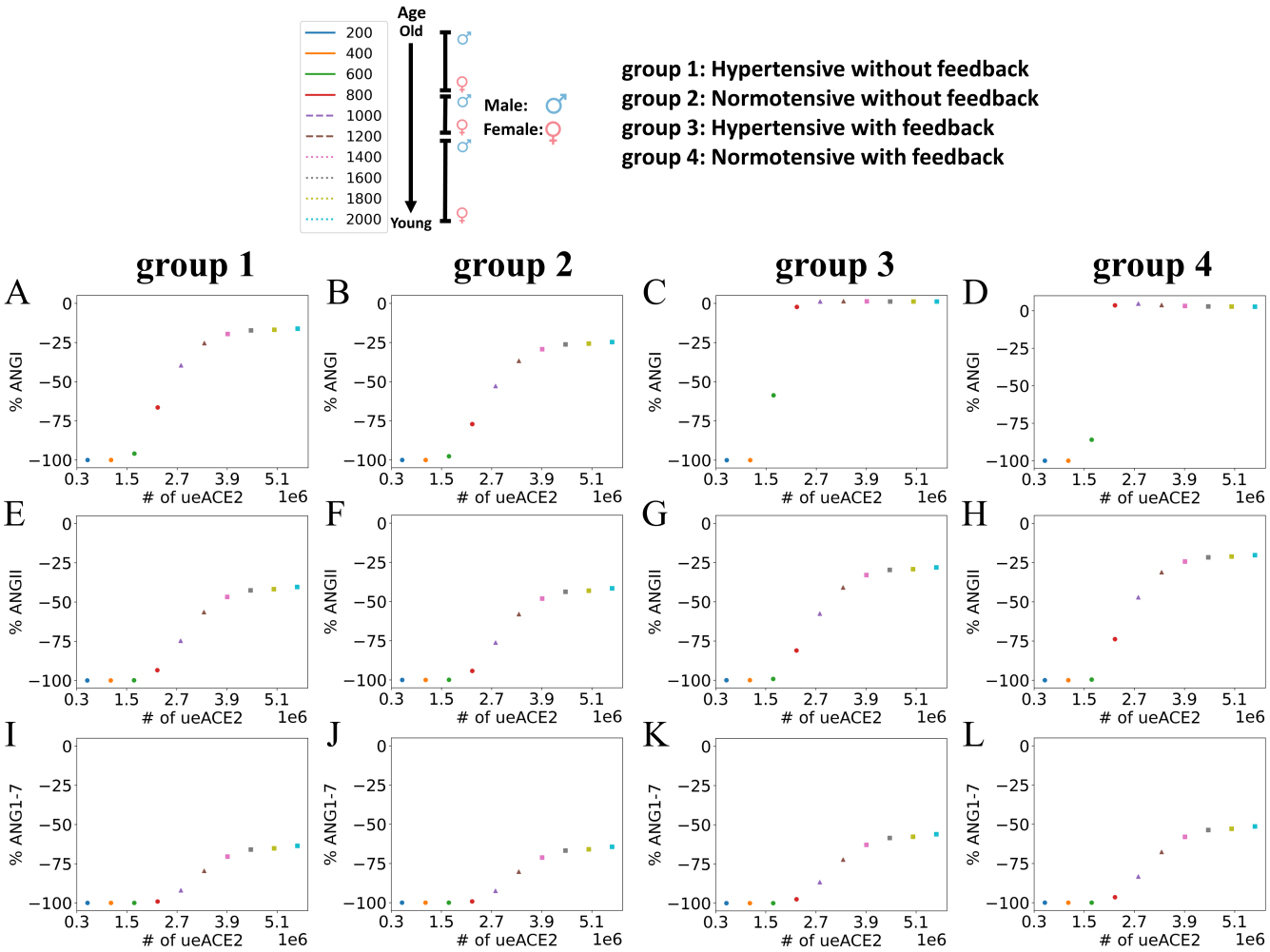


Fig. 5: Dose-response of unbound external ACE2 ($ueACE2_0$) to RAS peptides at day 10 after SARS-CoV-2 infection. (A–D) ANGI, (E–H) ANGII, and (I–L) ANG1-7 for $ueACE2_0$ ranges of 200–2000. Group 1: hypertensive patients with no feedback from ANGII·AT1R to renin, Group 2: normotensive patients with no feedback from ANGII·AT1R to renin, Group 3: hypertensive patients with feedback from ANGII·AT1R to renin, and Group 4: normotensive patients with feedback from ANGII·AT1R to renin. Groups represent each column.

### *3.5. Sensitivity analysis*

The dynamic local sensitivity analysis for parameters was conducted to quantify the sensitivity of model output ANGII with input parameters. The analyses were performed for the parameters: $\beta$, $k_A$, $c_A$, $c_R$, $k_{ACE2\cdot ANGII}$, $k_{ACE2}$, $c_{APA}, c_{AT1}$, and $c_{AT2}$. We ran the sensitivity analyses using $m_S = [0.1, 0.3, 0.5, 0.7, 0.9, 1.1, 1.5, 2, 5, 10]$ as inputs. Fig. 6 shows the dynamic local sensitivity for parameters for hypertensive patients with no feedback from ANGII·AT1R to renin (Group 1). The sensitivity analysis of ANGII showed parameters $\beta$, $c_A$, and $k_{ACE2\cdot ANGII}$ changed the steady state of ANGII before infection. $c_A$ modulated ANGII response positively and $k_{ACE2\cdot ANGII}$ modulated ANGII response negatively before infection. After the infection, $c_A$ and $k_{ACE2\cdot ANGII}$ modulated ANGII response positively.

### *3.6. Dynamics of fibrosis model with patient differences in RAS network*

Multiple studies identified a reduction in ACE2 and an increase in ANGII as regulators of excess collagen deposition and fibrosis [23–27]. Here, we assumed that the reduction of ACE2 in the lung tissue contributes to a surplus of ANGII (unconverted ANGII) at a systemic level and increases the systemic concentration of ANGII. In a study, Liu et al. [2] collected plasma samples and demographic data from 55 SARS-CoV-2-positive patients. They reported increased plasma ANGII above the normal range of plasma ANGII (25–129 pg mL$^{-1}$), mainly in critically ill patients. The measured range of ANGII in the critically ill patients group was 149.7 (137.8, 165.1) pg mL$^{-1}$ where the

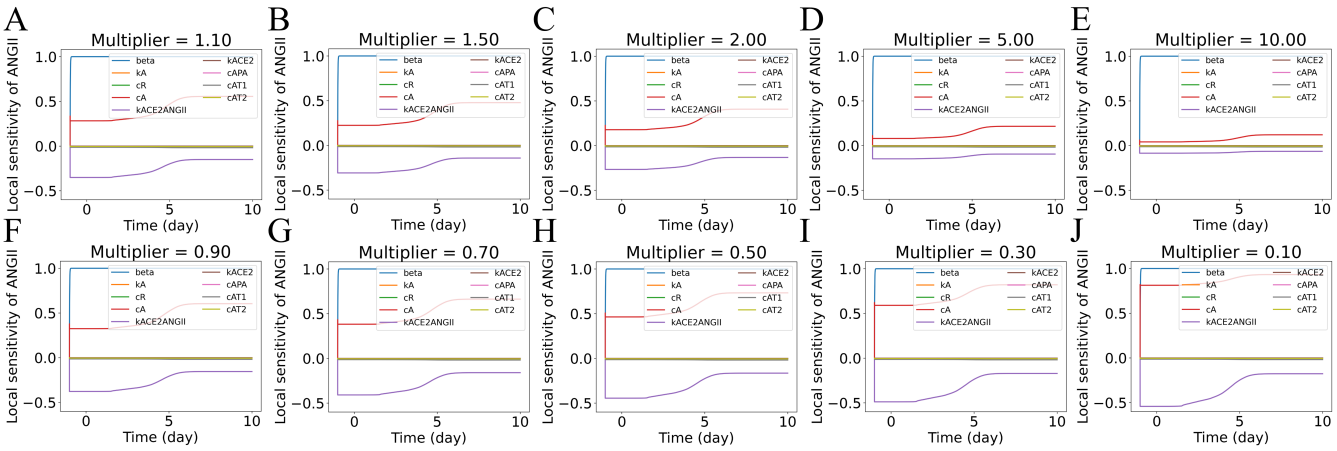


Fig. 6: Dynamic local sensitivity analysis of parameters for ANGII for hypertensive patients with no feedback from ANGII·AT1R to renin. The parameters are multiplied by a multiplier ($m_S$), increasing in the top row: (A) 1.1, (B) 1.5, (C) 2, (D) 5, (E) 10, and decreasing in the bottom row: (F) 0.9, (G) 0.7, (H) 0.5, (I) 0.3, and (J) 0.1.

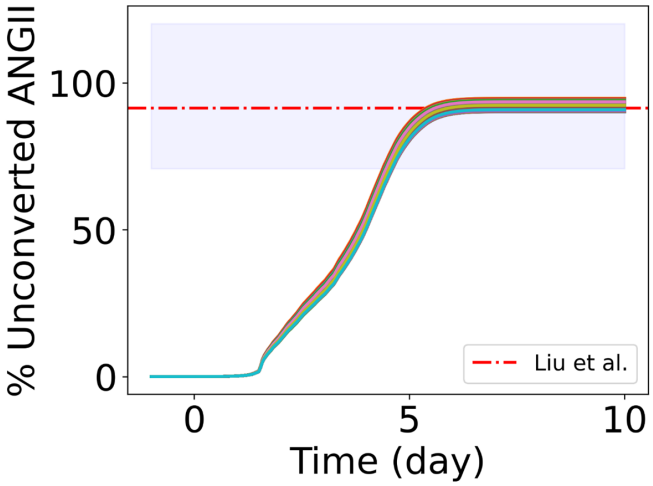


Fig. 7: Dynamics of unconverted ANGII for 1000 virtual patients. The dashed line and shaded area represent experimentally reported increase in ANGII in critically ill patients [2] from the mean ANGII of the normal range.

values represent mean (lower bound, upper bound). So, from the mean of the normal range of ANGII (77 pg mL$^{-1}$), ANGII in the critically ill patients group increased by 94.4%(79%, 114.4%). Here, we assumed that the increase in ANGII in critically ill patients from the mean value of ANGII of normal patients is due to the dysregulation in ACE2. Unconverted ANGII in our model represents the difference in ANGII between baseline ACE2 ($ACE2(t_i)$) and reduced ACE2 dynamics considering cell death ($ACE2(t > t_i)$, Eq. (13) in Section 2.1.3). Fig. 7 shows the percentage unconverted ANGII increase from baseline with initial RAS peptide concentration variations for 1000 virtual patients sampled in Section 3.3. We predicted a similar increase in unconverted ANGII at $ueACE2_0 = 1000$ as the experimental observations of Liu et al. [2].

Then, we considered simplified first-order reaction kinetics to account for ANGII-induced TGF-β production from unconverted ANGII. The *in vitro* experiments of Lai et al. [55] showed increased TGF-β concentration in human mesangial cells (279–630 pg mL$^{-1}$) with increasing ANGII ranges (0–10$^{-7}$ M). Singh et al. [56] also observed changes in TGF-β concentration in the range 0.827–1.65 ng mL$^{-1}$ with changes of ANGII from the control condition to 10$^{-8}$ M in their *in vitro* experiments on human mesangial cells. The changes in ANGII in our model occur at a much lower range compared to these experiments. However, similar experiments in lung cells could be used to parameterize $k_T$. We varied $k_T$ $1\times10^{-4}$–$10\times10^{-4}$ ng mL min$^{-1}$ fmol$^{-1}$ for hypertensive patients with no feedback from ANGII·AT1R to renin and observed linear changes in immune cells and collagen dynamics with variations in $k_T$ (Fig. S7). Our

goal was to keep TGF-β concentration within the range of experimental observations (0–10 ng/mL) where the TGF-β-dependent functions for fibroblasts were defined [19–21]. We selected $k_T = 5 \times 10^{-4}$ ng mL min$^{-1}$ fmol$^{-1}$ to simulate the dynamics of immune cells and collagen for different age and sex groups. Fig. 8 shows the dynamics

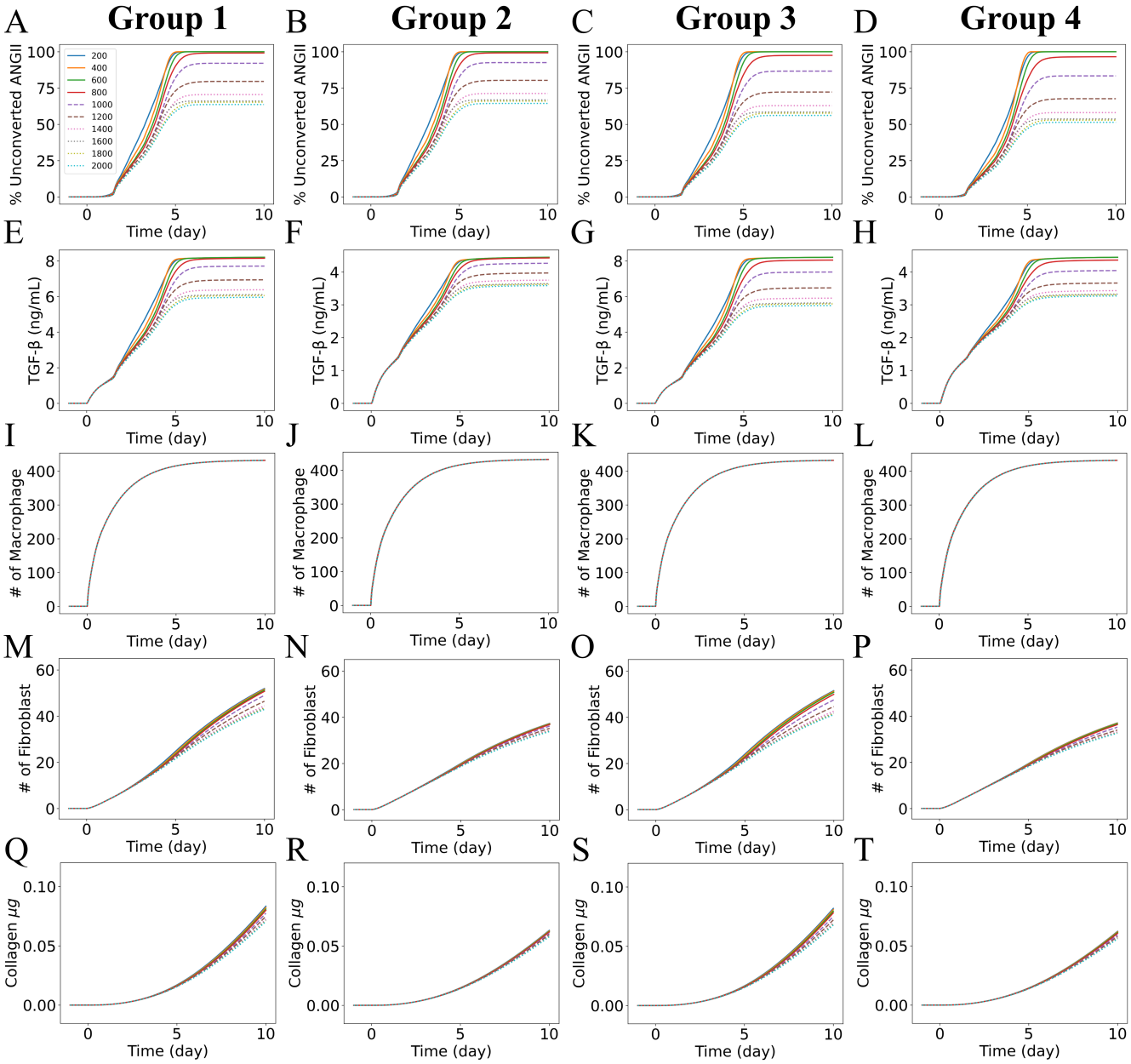


Fig. 8: Dynamics of unconverted (A–D) ANGII, (E-H) TGF-β, (I–L) macrophages, (M–P) fibroblasts, and (O–T) collagen. **Group 1:** hypertensive patients with no feedback from ANGII·AT1R to renin, **Group 2:** normotensive patients with no feedback from ANGII·AT1R to renin, **Group 3:** hypertensive patients with feedback from ANGII·AT1R to renin, and **Group 4:** normotensive patients with feedback from ANGII·AT1R to renin. Groups represent each column.

of fibrosis model species: unconverted ANGII, TGF-β, macrophages, fibroblasts, and collagen. Fig. S8 shows the dose-response of $ueACE2_0$ to immune model species at ten days post infection for four patient groups described in the Section 3.4. Our simulated results show increased macrophage and fibroblast populations and increased collagen deposition. However, we observed slight variations with aging in both sexes.

### *3.7. Limitations*

Our earlier COVID-19 tissue fibrosis model [19] identified M2 macrophages as the key regulators for fibrosis. In this model, we only used experimental data of TGF-β-dependent macrophage recruitment for up to 1 ng mL$^{-1}$

and assumed a constant response from 1–10 ng $mL^{-1}$ (Fig. S1). So, there is a need for experimental studies on TGF-β-dependent macrophage recruitment for TGF-β ranges of 1–10 ng $mL^{-1}$ to remove this assumption in our model, which may enhance the effect of patient differences. Although the current model predicted the variations in RAS peptides depending on age and sex, the effect of patient differences is modest for the dynamics of collagen (submodel 3). However, we observed variations in collagen area fraction depending on age and sex in our COVID-19 tissue model (submodel 1). Fig. S9 shows variations in the collagen area fraction depending on age and sex, and the variations increase from day 10 to day 15. Currently, we are running the COVID-19 tissue model and RAS model sequentially. Coupling the additional systemic influx of immune cells due to dysregulation in RAS may better simulate the patient differences in collagen deposition.

## 4. Conclusions

Heterogeneity in the severity of COVID-19 disease depends on the patient-specific premorbid conditions, age, and sex differences. We developed an integrated mathematical model to investigate and quantify the effect of these heterogeneous factors on RAS during COVID-19. We identified viral-infection induced cell death as a major reduction source of ACE2 and did not observe any significant difference due to viral-bound ACE2. We observed increased disease severity with aging and significant variations between male and female patients in the older and middle-aged groups. Our results predicted the mechanisms for conflicting RAS alterations from two previous experimental studies. We also predicted systemic immune recruitment and collagen deposition due to RAS alteration during COVID-19. Our model may find application in calibrating patent-specific local and systemic regulations of RAS with bleomycin-induced tissue fibrosis model and autopsy and biopsy tissue samples.

## 5. Acknowledgments

This work was supported by the National Institutes of Health grant R35 GM133763 and the University at Buffalo, and the Center for Computational Research at the University at Buffalo. We thank the scientific community for model feedback, including Paul Macklin, Michael Getz, Amber M. Smith, Thomas Hillen, and Yafei Wang.

## 6. Supplementary material

Supplementary material associated with this article can be found in the online version.

## References

[1] A. Kutz, A. Conen, C. Gregoriano, S. Haubitz, D. Koch, O. Domenig, L. Bernasconi, B. Mueller, P. Schuetz, Renin-angiotensin-aldosterone system peptide profiles in patients with COVID-19, European Journal of Endocrinology 184 (2021) 543–552.

[2] N. Liu, Y. Hong, R. G. Chen, H. M. Zhu, High rate of increased level of plasma angiotensin II and its gender difference in COVID-19: an analysis of 55 hospitalized patients with COVID-19 in a single hospital, WuHan, China, Journal of Clinical Toxicology 11 (2021) S16:001.

[3] F. L. Martins, C. A. Tavares, P. A. Malagrino, T. Rentz, A. Benetti, T. M. Rios, G. M. Pereira, B. Caramelli, S. K. Teixeira, J. E. Krieger, et al., Sex differences in the lung ACE/ACE2 balance in hypertensive rats, Bioscience Reports 41 (2021) BSR20211201.

[4] P. Pagliaro, C. Penna, ACE/ACE2 ratio: a key also in 2019 coronavirus disease (Covid-19)?, Frontiers in Medicine 7 (2020) 335.

[5] L. M. Hilliard, A. K. Sampson, R. D. Brown, K. M. Denton, The "his and hers" of the renin-angiotensin system, Current Hypertension Reports 15 (2013) 71–79.

[6] Y. Liu, Y. Yang, C. Zhang, F. Huang, F. Wang, J. Yuan, Z. Wang, J. Li, J. Li, C. Feng, et al., Clinical and biochemical indexes from 2019-nCoV infected patients linked to viral loads and lung injury, Science China Life Sciences 63 (2020) 364–374.

[7] H. Zhang, W. Shang, Q. Liu, X. Zhang, M. Zheng, M. Yue, Clinical characteristics of 194 cases of COVID-19 in Huanggang and Taian, China, Infection 48 (2020) 687–694.

[8] U. Kintscher, A. Slagman, O. Domenig, R. Röhle, F. Konietschke, M. Poglitsch, M. Möckel, Plasma angiotensin peptide profiling and ACE (angiotensin-converting enzyme)-2 activity in COVID-19 patients treated with pharmacological blockers of the renin-angiotensin system, Hypertension 76 (2020) e34–e36.

[9] K. D. Pendergrass, N. T. Pirro, B. M. Westwood, C. M. Ferrario, K. B. Brosnihan, M. C. Chappell, Sex differences in circulating and renal angiotensins of hypertensive mRen. lewis but not normotensive Lewis rats, American Journal of Physiology-Heart and Circulatory Physiology 295 (2008) H10–H20.

[10] X. Xudong, C. Junzhu, W. Xingxiang, Z. Furong, L. Yanrong, Age-and gender-related difference of ACE2 expression in rat lung, Life Sciences 78 (2006) 2166–2171.

[11] U. Bastolla, Mathematical model of SARS-Cov-2 propagation versus ACE2 fits COVID-19 lethality across age and sex and predicts that of SARS, Frontiers in Molecular Biosciences 8 (2021) 676.

[12] W. Miesbach, Pathological role of angiotensin II in severe COVID-19, TH Open 4 (2020) e138–e144.

[13] J. Yim, H. H. Lim, Y. Kwon, COVID-19 and pulmonary fibrosis: therapeutics in clinical trials, repurposing, and potential development, Archives of Pharmacal Research 44 (2021) 499–513.

[14] J. Wigén, A. Löfdahl, L. Bjermer, L. E. Rendin, G. Westergren-Thorsson, Converging pathways in pulmonary fibrosis and Covid-19-the fibrotic link to disease severity, Respiratory Medicine X 2 (2020) 100023.

[15] A. M. Murphy, A. L. Wong, M. Bezuhly, Modulation of angiotensin II signaling in the prevention of fibrosis, Fibrogenesis & Tissue Repair 8 (2015) 1–7.

[16] R. P. Marshall, P. Gohlke, R. C. Chambers, D. C. Howell, S. E. Bottoms, T. Unger, R. J. McAnulty, G. J. Laurent, Angiotensin II and the fibroproliferative response to acute lung injury, American Journal of Physiology-Lung Cellular and Molecular Physiology 286 (2004) L156–L164.

[17] G. H. Gibbons, R. Pratt, V. J. Dzau, et al., Vascular smooth muscle cell hypertrophy vs. hyperplasia. Autocrine transforming growth factor-beta 1 expression determines growth response to angiotensin II, The Journal of Clinical Investigation 90 (1992) 456–461.

[18] S. Kagami, W. A. Border, D. E. Miller, N. A. Noble, et al., Angiotensin II stimulates extracellular matrix protein synthesis through induction of transforming growth factor-beta expression in rat glomerular mesangial cells, Journal of Clinical Investigation 93 (1994) 2431–2437.

[19] M. A. Islam, M. Getz, P. Macklin, A. N. Ford Versypt, An agent-based modeling approach for lung fibrosis in response to covid-19, PLoS Computational Biology 19 (2023) e1011741.

[20] M. Ceresa, A. L. Olivares, J. Noailly, M. A. González Ballester, Coupled immunological and biomechanical model of emphysema progression, Frontiers in Physiology 9 (2018) 388.

[21] Y. F. Jin, H. C. Han, J. Berger, Q. Dai, M. L. Lindsey, Combining experimental and mathematical modeling to reveal mechanisms of macrophage-dependent left ventricular remodeling, BMC Systems Biology 5 (2011) 1–14.

[22] L. Mecozzi, M. Mambrini, F. Ruscitti, E. Ferrini, R. Ciccimarra, F. Ravanetti, N. Sverzellati, M. Silva, L. Ruffini, S. Belenkov, et al., In-vivo lung fibrosis staging in a bleomycin-mouse model: a new micro-CT guided densitometric approach, Scientific Reports 10 (2020) 1–12.

[23] X. Li, M. Molina-Molina, A. Abdul-Hafez, V. Uhal, A. Xaubet, B. D. Uhal, Angiotensin converting enzyme-2 is protective but downregulated in human and experimental lung fibrosis, American Journal of Physiology-Lung Cellular and Molecular Physiology 295 (2008) L178–L185.

[24] G. Rey-Parra, A. Vadivel, L. Coltan, A. Hall, F. Eaton, M. Schuster, H. Loibner, J. Penninger, Z. Kassiri, G. Oudit, et al., Angiotensin converting enzyme 2 abrogates bleomycin-induced lung injury, Journal of Molecular Medicine 90 (2012) 637–647.

[25] K. Kuba, Y. Imai, S. Rao, H. Gao, F. Guo, B. Guan, Y. Huan, P. Yang, Y. Zhang, W. Deng, et al., A crucial role of angiotensin converting enzyme 2 (ACE2) in SARS coronavirus-induced lung injury, Nature Medicine 11 (2005) 875–879.

[26] Y. Imai, K. Kuba, S. Rao, Y. Huan, F. Guo, B. Guan, P. Yang, R. Sarao, T. Wada, H. Leong-Poi, et al., Angiotensin-converting enzyme 2 protects from severe acute lung failure, Nature 436 (2005) 112–116.

[27] L. Wang, Y. Wang, T. Yang, Y. Guo, T. Sun, Angiotensin-converting enzyme 2 attenuates bleomycin-induced lung fibrosis in mice, Cellular Physiology and Biochemistry 36 (2015) 697–711.

[28] J. Leete, S. Gurley, A. T. Layton, Modeling sex differences in the renin angiotensin system and the efficacy of antihypertensive therapies, Computers & Chemical Engineering 112 (2018) 253–264.

[29] F. Pucci, P. Bogaerts, M. Rooman, Modeling the molecular impact of SARS-CoV-2 infection on the renin-angiotensin system, Viruses 12 (2020) 1367.

[30] M. Sadria, A. T. Layton, Use of angiotensin-converting enzyme inhibitors and angiotensin II receptor blockers during the COVID-19 pandemic: a modeling analysis, PLoS Computational Biology 16 (2020) e1008235.

[31] C. Voutouri, M. R. Nikmaneshi, C. C. Hardin, A. B. Patel, A. Verma, M. J. Khandekar, S. Dutta, T. Stylianopoulos, L. L. Munn, R. K. Jain, In silico dynamics of COVID-19 phenotypes for optimizing clinical management, Proceedings of the National Academy of Sciences 118 (2021) e2021642118.

[32] P. Barbiero, P. Lió, The computational patient has diabetes and a COVID, arXiv preprint arXiv:2006.06435 (2020).

[33] A. N. Ford Versypt, G. K. Harrell, A. N. McPeak, A pharmacokinetic/pharmacodynamic model of ace inhibition of the renin-angiotensin system for normal and impaired renal function, Computers & Chemical Engineering 104 (2017) 311–322.

[34] M. R. Pilvankar, M. A. Higgins, A. N. Ford Versypt, Mathematical model for glucose dependence of the local renin-angiotensin system in podocytes, Bulletin of Mathematical Biology 80 (2018) 880–905.

[35] M. R. Pilvankar, H. L. Yong, A. N. Ford Versypt, A glucose-dependent pharmacokinetic/pharmacodynamic model of ace inhibition in kidney cells, Processes 7 (2019) 131.

[36] A. Ghaffarizadeh, R. Heiland, S. H. Friedman, S. M. Mumenthaler, P. Macklin, Physicell: An open source physics-based cell simulator for 3-D multicellular systems, PLoS Computational Biology 14 (2018) e1005991.

[37] M. Getz, Y. Wang, G. An, A. Becker, C. Cockrell, N. Collier, M. Craig, C. L. Davis, J. Faeder, A. N. Ford Versypt, T. Mapder, J. F. Gianlupi1, J. A. Glazier, S. Hamis, R. Heiland, T. Hillen, D. Hou, M. A. Islam, et al., Rapid community-driven development of a SARS-CoV-2 tissue simulator, BioRxiv preprint DOI: 10.1101/2020.04.02.019075v3 (2020).

[38] M. Getz, Y. Wang, G. An, A. Becker, C. Cockrell, N. Collier, M. Craig, C. L. Davis, J. Faeder, A. N. Ford Versypt, T. Mapder, J. F. Gianlupi1, J. A. Glazier, S. Hamis, R. Heiland, T. Hillen, D. Hou, M. A. Islam, et al., Iterative community-driven development of a SARS-CoV-2 tissue simulator, BioRxiv preprint DOI: 10.1101/2020.04.02.019075v5 (2021).

[39] A. L. Jenner, R. A. Aogo, S. Alfonso, V. Crowe, X. Deng, A. P. Smith, P. A. Morel, C. L. Davis, A. M. Smith, M. Craig, COVID-19 virtual patient cohort suggests immune mechanisms driving disease outcomes, PLoS Pathogens 17 (2021) e1009753.

[40] H. Roca-Ho, M. Riera, V. Palau, J. Pascual, M. J. Soler, Characterization of ACE and ACE2 expression within different organs of the NOD mouse, International Journal of Molecular Sciences 18 (2017) 563.

[41] K. M. Hallow, A. Lo, J. Beh, M. Rodrigo, S. Ermakov, S. Friedman, H. de Leon, A. Sarkar, Y. Xiong, R. Sarangapani, et al., A model-based approach to investigating the pathophysiological mechanisms of hypertension and response to antihypertensive therapies: extending the Guyton model, American Journal of Physiology-Regulatory, Integrative and Comparative Physiology 306 (2014) R647–R662.

[42] W. Hao, C. Marsh, A. Friedman, A mathematical model of idiopathic pulmonary fibrosis, PLoS One 10 (2015) e0135097.

[43] A. B. Roberts, M. B. Sporn, R. K. Assoian, J. M. Smith, N. S. Roche, L. M. Wakefield, U. I. Heine, L. A. Liotta, V. Falanga, J. H. Kehrl, Transforming growth factor type beta: rapid induction of fibrosis and angiogenesis in vivo and stimulation of collagen formation in vitro, Proceedings of the National Academy of Sciences 83 (1986) 4167–4171.

[44] R. A. Ignotz, J. Massague, Transforming growth factor-beta stimulates the expression of fibronectin and collagen and their incorporation into the extracellular matrix, Journal of Biological Chemistry 261 (1986) 4337–4345.

[45] S. M. Wahl, D. A. Hunt, L. M. Wakefield, N. McCartney-Francis, L. M. Wahl, A. B. Roberts, M. B. Sporn, Transforming growth factor type beta induces monocyte chemotaxis and growth factor production, Proceedings of the National Academy of Sciences 84 (1987) 5788–5792.

[46] A. Katsurada, Y. Hagiwara, K. Miyashita, R. Satou, K. Miyata, N. Ohashi, L. G. Navar, H. Kobori, Novel sandwich ELISA for human angiotensinogen, American Journal of Physiology-Renal Physiology 293 (2007) F956–F960.

[47] M. C. Chappell, Biochemical evaluation of the renin-angiotensin system: the good, bad, and absolute?, American Journal of Physiology-Heart and Circulatory Physiology 310 (2016) H137–H152.

[48] J. C. Sullivan, P. Rodriguez-Miguelez, M. A. Zimmerman, R. A. Harris, Differences in angiotensin (1-7) between men and women, American Journal of Physiology-Heart and Circulatory Physiology 308 (2015) H1171–H1176.

[49] J. Nussberger, D. B. Brunner, B. Waeber, H. R. Brunner, Specific measurement of angiotensin metabolites and in vitro generated angiotensin II in plasma, Hypertension 8 (1986) 476–482.

[50] A. Rohatgi, Webplotdigitizer: Version 4.6, 2022. URL: `https://automeris.io/WebPlotDigitizer`.

[51] A. Ghaffarizadeh, S. H. Friedman, P. Macklin, BioFVM: an efficient, parallelized diffusive transport solver for 3-D biological simulations, Bioinformatics 32 (2016) 1256–1258.

[52] M. A. Islam, A. N. Ford Versypt, covid19fibrosis v1.1. DOI: 10.5281/zenodo.8432550, 2023. URL: `https://github.com/ashleefv/covid19fibrosis`.

[53] M. A. Islam, A. N. Ford Versypt, covid19fibrosisRAS DOI: 10.5281/zenodo.10674325, 2024. URL: `https://github.com/ashleefv/covid19fibrosisRAS`.

[54] B. Neubauer, J. Schrankl, D. Steppan, K. Neubauer, M. L. Sequeira-Lopez, L. Pan, R. A. Gomez, T. M. Coffman, K. W. Gross, A. Kurtz, et al., Angiotensin II short-loop feedback: is there a role of Ang II for the regulation of the renin system in vivo?, Hypertension 71 (2018) 1075–1082.

[55] K. N. Lai, S. C. Tang, J.-Y. Guh, T.-D. Chuang, M. F. Lam, L. Y. Chan, A. W. Tsang, J. C. Leung, Polymeric IgA1 from patients with IgA nephropathy upregulates transforming growth factor-$\beta$ synthesis and signal transduction in human mesangial cells via the renin-angiotensin system, Journal of the American Society of Nephrology 14 (2003) 3127–3137.

[56] R. Singh, N. Alavi, A. K. Singh, D. J. Leehey, Role of angiotensin II in glucose-induced inhibition of mesangial matrix degradation, Diabetes 48 (1999) 2066–2073.